16

Spectropolarimetric Imaging Techniques with Compressive Sensing

Fernando Soldevila[1], Esther Irles[1], Vicente Durán[1,2], Pere Clemente[1,3], Mercedes Fernández-Alonso[1,2], Enrique Tajahuerce[1,2] and Jesús Lancis[1,2]
[1]*GROC·UJI, Departament de Física, Universitat Jaume I, Spain*
[2]*Institut de Noves Tecnologies de la Imatge (INIT), Universitat Jaume I, Spain*
[3]*Servei Central d'Instrumentació Científica, Universitat Jaume I, Spain*

16.1 Chapter Overview

The information that the human eye can provide is limited. Although we are able to see in a wide range of distances, under different light conditions, and in a relatively broad spectral range, in many applications it is necessary to acquire information far beyond the limits imposed by the human eye. To this end, a great variety of image techniques have been developed [1]. As an archetypical example, microscopy, which is essential in fields like biology or medicine, provides a tool for obtaining high-resolution images of very close objects [2]. Many of these imaging techniques share a common feature: they measure the intensity of the light coming from the scene under consideration. However, it is sometimes required to measure other physical quantities, like the phase of the optical field, its spectral content, or its polarization state. The spectral content of a sample is normally used to obtain information about its material components. Polarization, that is, the knowledge of the vector nature of light, gives information about surface features such as shape, shading, and roughness of an object [3]. Advanced imaging techniques make it possible to acquire multi-dimensional images, which provide information not only about the spatial distribution of intensity but also about the previously mentioned primary physical quantities associated with an optical field.

Multi-dimensional Imaging, First Edition. Edited by Bahram Javidi, Enrique Tajahuerce and Pedro Andrés.
© 2014 John Wiley & Sons, Ltd. Published 2014 by John Wiley & Sons, Ltd.

In general, the measurement of multi-dimensional images involves the acquisition of a huge amount of information, which causes both storage and transmission difficulties [4]. In addition, techniques such as multispectral or hyperspectral imaging, require a sequential acquisition of images in the spectral domain, leading to a dramatic increase in measurement time. A recent approach to hyperspectral and polarimetric imaging is based on the use, respectively, of miniaturized spectral and polarimetric filters [5,6] that are incorporated to each pixel of the sensor, which allows acquiring multi-dimensional images in one shot. However, the development of such systems implies the use of high-end micro-optical components.

In this chapter, we describe several single-pixel multi-dimensional imaging systems based on *compressive sensing* (CS), a new sampling paradigm that has revolutionized data acquisition protocols, enabling us to start the signal compression at the measurement stage. In Section 16.2 we show how single-pixel imaging techniques work and how CS can boost their performance. In Sections 16.3 to 16.5 we describe single-pixel architectures that use off-the-shelf components in the fields of polarimetry, multispectral imaging, and spectropolarimetry.

16.2 Single-Pixel Imaging and Compressive Sensing

The operation principle of single-pixel imaging can be briefly described as follows. Let us consider a sample object, whose N-pixel image is arranged in an $N \times 1$ column vector, $\mathbf{x}$. That image can be expressed in terms of a basis of functions, $\mathbf{\Psi} = \{\mathbf{\Psi}_\ell\}$ (ℓ=*1, …, N*). In mathematical terms, $\mathbf{x} = \mathbf{\Psi} \cdot \mathbf{s}$, where $\mathbf{\Psi}$ is a $N \times N$ matrix that has the vectors $\{\mathbf{\Psi}_\ell\}$ as columns and $\mathbf{s}$ is the $N \times 1$ vector which contains the expansion coefficients of $\mathbf{x}$ in the chosen basis. Single-pixel cameras exploit the fact that those coefficients can be measured by using detectors with no spatial resolution. The acquisition process is governed by a spatial light modulator (SLM), which generates a set of patterns directly related to the selected basis. The irradiance corresponding to the inner product between the patterns and the object provides the coefficients of the image expansion.

In recent years, the introduction of CS has dramatically improved the performance of these single-pixel architectures. CS exploits the fact that natural images tend to be sparse, that is, only a small set of the expansion coefficients is nonzero when a suitable basis is chosen [7]. In this way, images can be retrieved without measuring all the projections of the object on the chosen basis. The mathematical formulation behind CS ensures that the object under study, $\mathbf{x}$, can be reconstructed from just a random subset of the expansion coefficients that make up $\mathbf{s}$. To this end, we randomly choose M different functions of the basis ($M < N$) and measure the projections of the object. This process can be expressed in matrix form as

$$\mathbf{y} = \mathbf{\Phi} \cdot \mathbf{x} = \mathbf{\Phi}(\mathbf{\Psi} \cdot \mathbf{s}) = \mathbf{\Theta} \cdot \mathbf{s}, \tag{16.1}$$

where $\mathbf{y}$ is a $M \times 1$ vector which contains the measured projections and $\mathbf{\Phi}$ is a $M \times N$ matrix called sensing matrix. Each row of $\mathbf{\Phi}$ is a function of $\mathbf{\Psi}$ chosen randomly, and the product of $\mathbf{\Phi}$ and $\mathbf{\Psi}$ gives the matrix $\mathbf{\Theta}$ acting on $\mathbf{s}$. If the chosen basis is orthonormal, every row of $\mathbf{\Theta}$ randomly selects a unique element of $\mathbf{s}$. As $M < N$, the underdetermined matrix relation obtained after the measurement process is resolved through an off-line algorithm. The best approach to recover the object is based on the minimization of the ℓ_1-norm of $\mathbf{s}$ subjected to the constrain given by Eq. (16.1), that is, that the solution given by the algorithm has to be compatible with the performed measurements. In this case, the proposed reconstruction $\mathbf{x}^*$ is given by the optimization program

$$\min_{\mathbf{x}^*} \|\boldsymbol{\Psi}^{-1}\mathbf{x}^*\|_{\ell_1} \text{ subject to } \boldsymbol{\Phi}\mathbf{x}^* = \mathbf{y}. \tag{16.2}$$

In the experiments described in this paper, the chosen basis is a family of binary intensity patterns derived from the Walsh–Hadamard basis. This basis has proved to be suitable for single-pixel architectures due to being easily implemented on a SLM. A Walsh–Hadamard matrix of order N ($\mathbf{H}_N$) is a $N \times N$ matrix with ±1 entries that satisfies $\mathbf{H}_N^T\mathbf{H}_N = N \cdot \mathbf{I}_N$, where $\mathbf{I}_N$ is the identity matrix and $\mathbf{H}_N^T$ denotes transposed matrix. Walsh–Hadamard matrices form an orthonormal basis that was first proposed in image coding and transmission techniques [8]. By shifting and rescaling the different $\mathbf{H}_N$, it is possible to generate binary waveforms taking values 0 or 1 that can be simply encoded onto the SLM as an intensity modulation.

A suitable SLM for a single-pixel camera is a display formed by voltage-controlled liquid-crystal (LC) cells, such as those found in video projection systems [9]. Another option is a digital micromirror device (DMD), composed of an array of micromirrors that can rotate between two positions. In this way, only selected portions of the incoming light beam are reflected in a given direction [10]. Both devices are used in the different optical systems described in the following sections. Regarding detection, in general, a photodiode is used as single-pixel camera, which measures the irradiance of the light coming from an object for each pattern generated by the SLM. In the optical systems described in this chapter other single-pixel detectors, such as a beam polarimeter or a fiber spectrometer, are used.

16.3 Single-Pixel Polarimetric Imaging

Polarimetric imaging (PI) has the aim of measuring spatially resolved polarization properties of a light field, an object, or an optical system [11]. These properties are usually the Stokes parameters of light (passive imaging polarimeters) or the Mueller matrix that characterizes a sample or a system (active imaging polarimeters). The use of PI includes a great variety of optical applications, like scene analysis, target detection [3], polarization-sensitive microscopy [12], or segmentation of rough surfaces [13], among others. Polarimetric techniques have been used in the field of biomedical imaging for enhanced visualization of biological samples at different depths [14], as well as *in vivo* detection and diagnosis of cancerous tumors in tissues [15,16]. PI can be also combined with optical coherence tomography [17] and ophthalmic adaptive optics [18].

In this chapter, we describe how the concept of single-pixel imaging by CS has been extended to the design of a passive polarimetric camera. In particular, we describe a PI system able to measure spatially resolved Stokes parameters by means of a commercial beam polarimeter [19]. This commercial beam polarimeter is designed for free-space and fiber-based measurements, and provides the state of polarization (SOP) of an optical beam as a whole; that is, without spatial resolution. The PI system exhibits high dynamic range (up to 70 dB), broad wavelength range, and high accuracy on the Poincaré sphere, thanks to the use of the beam polarimeter. This fact simplifies the design and optimization procedures of current polarimetric cameras based on pixelated image sensors [16,20]. A programmable SLM is at the heart of this imaging polarimeter. This modulator controls the time-multiplexed acquisition process required by a single-pixel imaging scheme. The amount of acquired data is minimized by the application of a CS algorithm, which implies a proper selection of light patterns generated by the SLM, in accordance with the theory briefly described in Section 16.2.

A *Stokes polarimeter* (SP) is a device that measures the irradiance of a light beam whose SOP is modulated by a *polarization state analyzer* (PSA). In the commercial SP used here, which is sketched in Fig. 16.1, the PSA is formed by two voltage-controlled liquid-crystal variable retarders (LCVR$_1$ and LCVR$_2$) and a polarizing beam splitter (PBS). Two photodiodes (PD$_1$ and PD$_2$) are respectively located at the output ports of the PBS. The sum of the signals of PD$_1$ and PD$_2$ gives the total irradiance I_0 impinging onto the SP, despite of slight (and measurable) losses. The application of the Stokes–Mueller formalism allows obtaining the SOP of the input light, which is given by the Stokes vector $(I_0, S_1, S_2, S_3)^T$. If the retardances of LCVR$_1$ and LCVR$_2$ are δ_1 and δ_2, respectively, the irradiance I_{PD} measured by one photodiode is given by

$$I_{PD}(\delta_1, \delta_2) = m_{00}(\delta_1, \delta_2) I_0 + \sum_{i=1}^{3} m_{0i}(\delta_1, \delta_2) S_i. \tag{16.3}$$

In this expression $m_{0k}(k = 0, \ldots, 3)$ are the voltage-dependent elements of the first row of the PSA Mueller matrix. A proper calibration process, usually performed by the manufacturer, can be used to determine these elements. The description of such a process is out of the scope of the present study [21]. By a sequential reconfiguration of the PSA, the SOP of the incoming light is derived through the measurement of at least three values of I_{PD}, together with the irradiance I_0. In commercial devices, the LCVRs perform a wide retardance sweep. In this way, the input SOP is obtained through a least-squares fitting routine to minimize measurement errors [22]. The quantities registered by the SP are usually the normalized version of the Stokes parameters, $\sigma_{\mathrm{i}} = S_{\mathrm{i}}/I_0 (i = 1, \ldots, 3)$. It should be noted that the retardance of the LCVRs strongly depends on the light frequency, so the device calibration is valid for a given wavelength and must be repeated if the light source spectrum is changed.

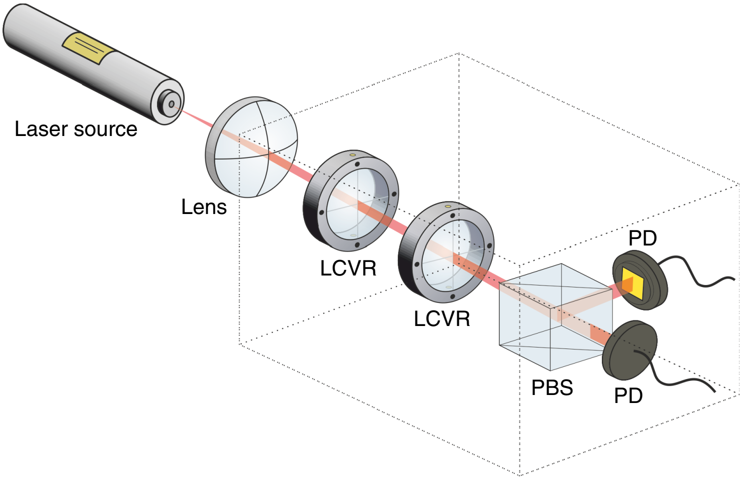

Figure 16.1 Scheme of the Stokes polarimeter acting as a single-pixel detector

A polarimetric detector with no spatial structure, such as the SP detector in Fig. 16.1, can be adapted to perform PI with the aid of the single-pixel architecture discussed on Section 16.2. The idea is simple: the problem of measuring a spatial-dependent Stokes vector is equivalent to resolving three times the CS algorithm of single-pixel imaging. This is possible because the linearity of Eq. (16.3) implies that each Stokes parameter S_i^{SP} provided by the SP is the sum of the values taken by S_i at each point of the input light beam. As a consequence, the measurement process expressed by Eq. (16.1) can be separately applied to each Stokes parameter whose spatial distribution (described by an N-pixel matrix) is recovered using $M < N$ polarimetric measurements. A layout of the PI system is depicted in Fig. 16.2. A collimated (unpolarized) laser beam passes through an LC-SLM, programmed to generate a set of intensity patterns. Just after the modulator there is a polarization object (PO), which produces a space-variant Stokes vector. As an LC-SLM is a polarization-dependent device; it is sandwiched between properly oriented linear polarizers (P_1 and P_2), so the object is illuminated with linearly polarized light. The light emerging from the object is guided to the SP by means of an afocal optical system, like an inverted beam expander, which fits the beam width to the typically small entrance window of the SP. This coupling optic ensures that all the light emerging from the object is collected by the SP and it preserves the normal incidence, which contributes to the optimal performance of the polarimeter.

The light source used in this experiment was an He-Ne laser emitting at 632.8 nm. The LC-SLM was a transmissive twisted nematic LCD (TNLCD) with SVGA resolution (800 × 600 pixels) and a pixel pitch of 32 μm. To reach an intensity modulation regime, the LC-SLM was sandwiched between two linear polarizers, respectively oriented parallel and normal to the input molecular director of the TNLCD, which was previously determined by a polarimetric technique [23]. In this configuration, the LC-SLM worked as a spatial intensity modulator. Pixels were individually addressed by sending gray-level images to the TNLCD. Each gray level corresponded to a transmitted intensity level, ranging from the dark state (extinction) to the bright state (maximum transmission).

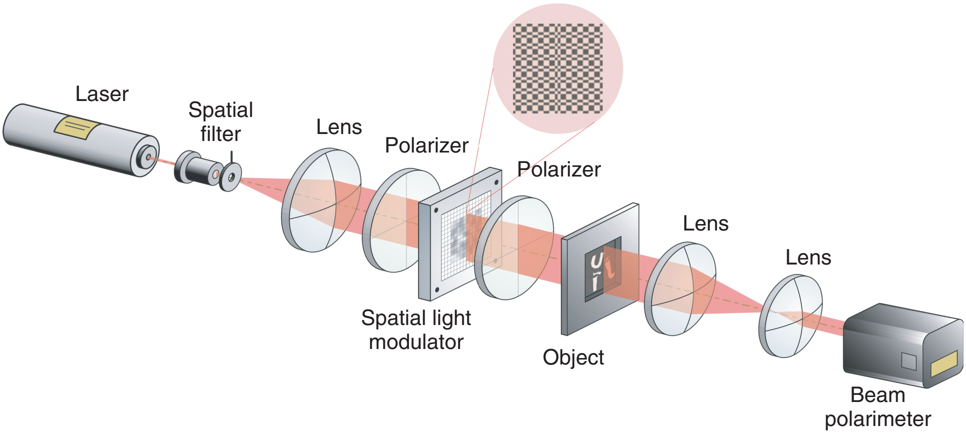

Figure 16.2 Experimental setup for the polarimetric single-pixel camera. One of the binary intensity patterns displayed by the SLM is also shown

Table 16.1 Technical specifications of the polarimetric camera

Wavelength	632.8 nm
Image resolution	64 × 64 pixels
Compression ratio	3:1
Pixel pitch	64 μm

In order to perform CS, the Walsh–Hadamard functions were chosen as the reconstruction basis $\mathbf{\Psi}$. This election was particularly useful because the intensity patterns $\{\Phi_m\}$ generated by the TNLCD were binary masks (see Fig. 16.2). The corresponding images addressed to the display had a resolution of 64 × 64 cells, and the cell pitch was 64 μm. The number of binary patterns displayed onto the TNLCD was 1225, which represents ∼30% of the Nyquist criterion. Custom software written with LabVIEW was used to synchronize the SP with the modulator. These technical specifications are summarized in Table 16.1. For each realization, the values of the Stokes parameters $\{S_i^{SP}\}(i = 1, \ldots, 3)$, as well as the signals of PD_1 and PD_2, are measured. The maximum measurement rate of the SP (10 Stokes vectors per second) was the speed limiting factor, since the refreshing frequency of the TNLCD was 60 Hz.

The selected object, shown in Fig. 16.3(a), was a cellophane film, acting as linear retarder, attached to an amplitude mask, which reproduces the logotype of the university UJI. Linearly

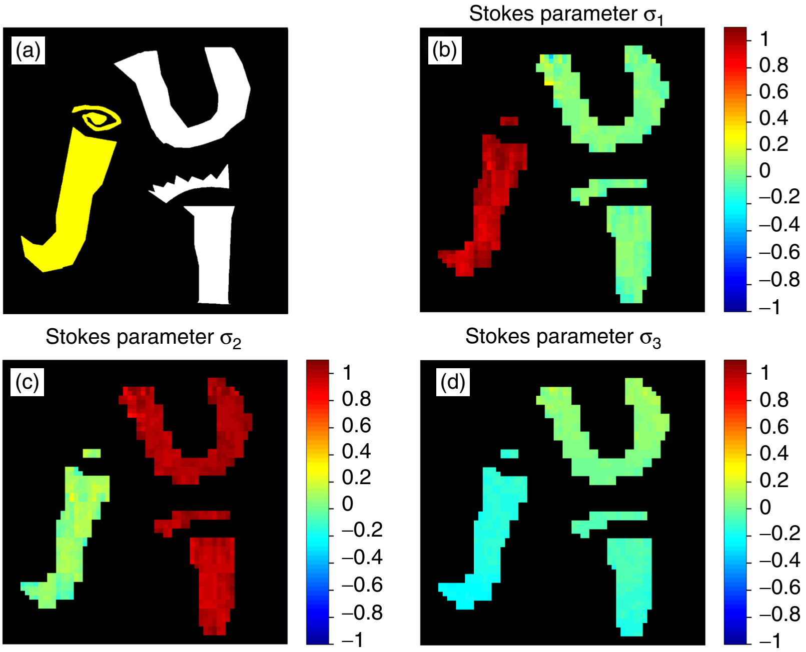

Figure 16.3 (a) High-resolution representation of the object under study, which is an amplitude mask representing the logo of the university UJI, with a cellophane film over the letter in gray shading (was yellow). Pseudocolored pictures showing the distribution of the Stokes parameters are shown in (b), (c), and (d). *Source*: V. Durán, P. Clemente, M. Fernández-Alonso, E. Tajahuerce, and J. Lancis 2012, Figure 3. Reproduced with permission from The Optical Society

polarized light emerging from the polarizer P_2 illuminated the object. An inhomogeneous polarization distribution was generated by covering just the capital letter J with cellophane. With the introduction of this element, the polarization of the light coming from this letter was approximately rotated by the cellophane film. The parameters of the polarization ellipse (the azimuth α and the ellipticity e) of the light passing through the J were measured by the SP (blocking the light emerging from the other part of the object). For this measurement, the TNLCD was configured in its bright state. The results were $\alpha_J = 8.62°$ and $e_J = -0.07$. Repeating the process for letters U and I, the measured parameters were $\alpha_{U,I} = 42.22°$ and $e_{U,I} = 0.003$.

Figures 16.3(b)–N.3(d) show pseudocolor plots for the normalized Stokes parameters. These images exhibit a clear uniformity within the different parts of the object. The spatial distributions for α and e were calculated from the Stokes parameters through conventional expressions (see, for example, [24]). The mean values of the ellipse parameters for each part of the object were ($\langle \alpha_\mathrm{J} \rangle = 2.5° \pm 1.4°$, $\langle e_\mathrm{J} \rangle = -0.08 \pm 0.02$) and ($\langle \alpha_\mathrm{U,I} \rangle = 43.6° \pm 1.1°$, $\langle e_\mathrm{U,I} \rangle = -0.01 \pm 0.04$). The assigned uncertainties were the standard deviations of each distribution. These results were in good agreement with the values previously measured by the SP. The major discrepancy was found for $\alpha_J (\sim 6°)$, which only represents ~3% of the total range of values (from −90° to 90°) that can be taken by the azimuth.

These results demonstrate the possibility of performing spatially resolved Stokes polarimetry with the aid of CS. In particular, the system described here converts a commercial beam SP into a polarimetric imager. Although this system is based on liquid crystal elements, the method is valid for other types of polarimeters, provided that the selected device is itself spatially homogeneous, and the relationship between the measured signals and the Stokes parameters is linear, as in Eq. (16.3). Concerning the acquisition process, a TNLCD is used to project the intensity patterns over the object. Another possibility is to employ SLMs insensitive to polarization, like a DMD, as is done in the optical systems described in the following sections. The combination of DMDs with fast SPs may lead to the design of PI systems working at very high frequencies (~1 KHz), opening the door to near-real-time applications.

16.4 Single-Pixel Multispectral Imaging

Multispectral imaging (MI) is a useful optical technique that provides two-dimensional images of an object for a set of specific wavelengths within a selected spectral range [1]. Dispersive elements (prisms or gratings), filter wheels, or tunable band-pass filters, are typical components used in MI systems to acquire image spectral content [25]. Multispectral imaging provides both spatial and spectral information of an object and represents a powerful analysis tool in different scientific fields as medicine [26], pharmaceutics [27], astronomy [28], and agriculture [29]. In industry, new techniques have emerged that use VIS and NIR imaging to make quality and safety control, for example, in the detection of surface properties on fruits [30].

The second optical system described in this chapter is a CS imaging system able to provide spatially resolved information about the spectrum of the light reflected by an object [31]. A fiber spectrometer with no spatial resolution is used as a single-pixel detector. Now, the key element of the system that makes possible the CS acquisition process, is a digital micromirror device (DMD). The modulator sequentially generates a set of binary intensity patterns that sample the image of the object under consideration. The acquired data is subsequently processed to obtain a multispectral data cube.

A layout of the spectral camera is shown in Fig. 16.4(a). A white-light source illuminates a sample and a CCD camera lens images the object on a DMD, which is a reflective spatial light modulator that selectively redirects parts of an input light beam [32]. The DMD consists of an array of electronically controlled micromirrors, positioned over a CMOS memory cell, which can rotate about a hinge, as is schematically depicted in Fig. 16.4(b). The angular position of each micromirror admits two possible states (+12° and −12° respect to a common direction), depending on the binary state (logic 0 or 1) of the corresponding CMOS memory cell contents. As a consequence, light can be reflected at two angles depending on the signal applied to the mirror. The DMD used in this system is a Texas Instrument device (DLP Discovery 4100) with a resolution of 1920×1080 micromirrors, the panel size of the display is $0.95''$, the mirror pitch is $10.8\,\mu\text{m}$ and the fill factor is greater than 0.91. The optical axis of the "optical system 1" forms an angle with respect to the orthogonal direction to the DMD panel that approximately corresponds to twice the tilt angle of the device mirrors (24°). As is shown in Fig. 16.4(c), a micromirror oriented at +12° orthogonally reflects the light, appearing as a bright pixel (ON state). In their turn, micromirrors oriented at −12° work as dark pixels (OFF state). The light emerging from the bright pixels of the DMD is collected by "the optical system 2" (see Fig. 16.4a). This lens system couples the light into a silica multimode fiber with a diameter of $1000\,\mu\text{m}$, which is connected to a commercial concave grating spectrometer (Black Comet CXR-SR from Stellarnet). The spectral range of the fiber ranges from 220–1100 nm. The wavelength resolution of this spectrometer is 8 nm (with a slit of $200\,\mu\text{m}$) and the maximum *signal-to-noise ratio* (SNR) is 1000:1. Technical specifications for this setup are summarized in Table 16.2.

An example of spectral image with resolution 256×256 pixels was performed with a sample object composed of an unripe cherry tomato together with a red one. The illumination source was a xenon white light lamp. The Walsh–Hadamard patterns addressed to the DMD had $N = 65536$ unit cells. Each unit cell was composed of 2×2 DMD pixels. With this resolution, the number of measurements was chosen to be $M = 6561$, which corresponds to a compression rate of 10:1 ($M \approx 0.1N$). The integration time of each spectrometer measurement was 300 ms.

In order to determine the object spectral reflectance, a spectrum was taken from a white reference (Spectralon diffuse 99% reflectance target from Labsphere, Inc.) to normalize the measured spectra during the CS acquisition process. In the case of plants, the chlorophyll content in leaves can be recovered from the spectral reflectance [33,34]. The data collected by the spectrometer for wavelengths lower than 500 nm, clearly affected by noise, imposed an inferior boundary to the usable spectral range. The results of the CS reconstruction for 15 spectral channels are shown in Fig. 16.5 (Plate 26). The selected central wavelengths λ_0 in the visible spectrum (VIS) range from 510–680 nm. The bandwidth of each spectrum channel was 10 nm ($\lambda_0 \pm 5$ nm). The recovered images were pseudo-colored and the color assignment (the wavelength to RGB transform) was carried out with the aid of standard XYZ Color-Matching Functions [35]. The CS algorithm provided an acceptable reconstruction in the near-infrared spectrum, around 860 nm. This is presented by means of a gray-level image. Figure 16.5 also includes a RGB image of the object.

The quality of the images obtained with the single-pixel camera in Fig. 16.4(a) is evaluated by performing a multispectral imaging experiment, by sending Walsh–Hadamard patterns of

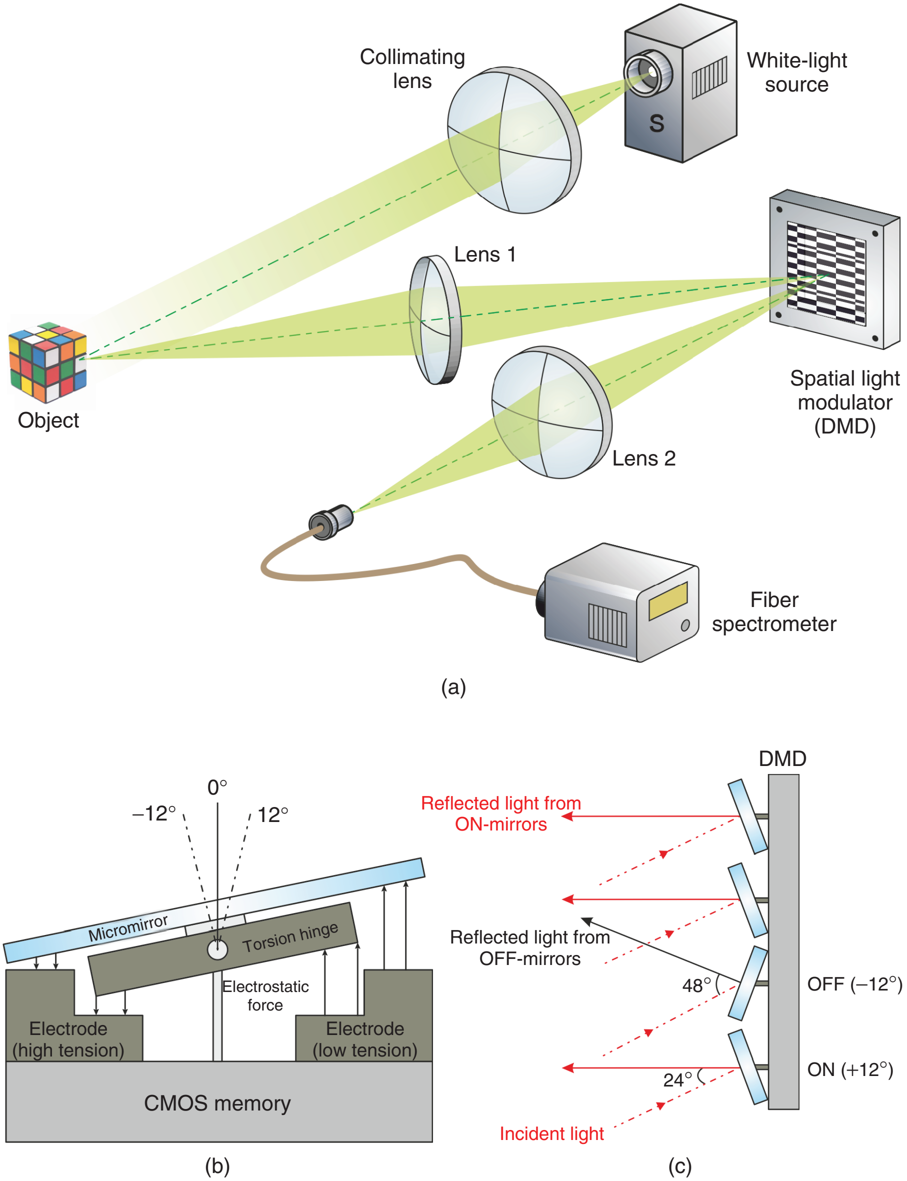

Figure 16.4 (a) Optical system for multispectral imaging using a single-pixel detector, (b) Individual DMD micromirror showed in the transverse view indicating its two possible orientations. (c) Working mode scheme of the DMD

Table 16.2 Technical specifications of the multispectral camera

Wavelength range	505–865 nm
Number of channels	15
Image resolution	256 × 256 pixels
Compression ratio	10:1
Integration time	300 ms
Pixel pitch	21.6 µm

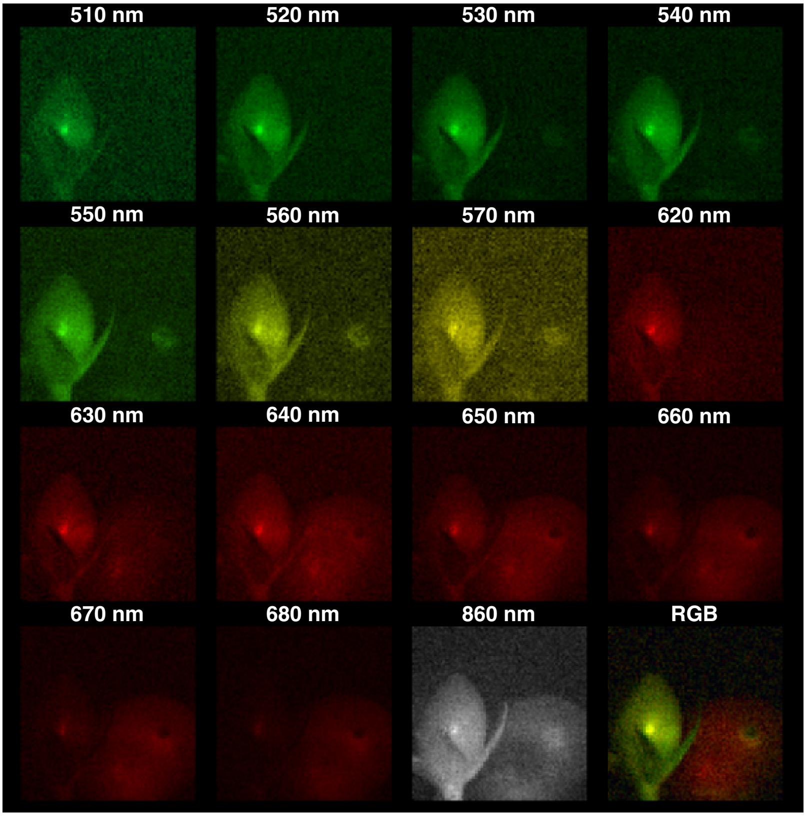

Figure 16.5 (Plate 26) Multispectral data cube reconstructed using CS. In the VIS band, the reflectance for each spectral channel is represented by means of a 256 × 256 pseudo-color image. In the NIR band we show a gray-scale representation. A colorful image of the scene made up from the conventional RGB channels is also included. *Source*: F. Soldevila, E. Irles, V. Durán, P. Clemente, M. Fernández-Alonso, E. Tajahuerce, and J. Lancis 2013, Figure 4. Reproduced with permission from Springer. *See plate section for the color version*

64×64 unit cells ($N = 4096$) to the modulator, each one composed of 8×8 DMD pixels. In this case, the sample scene is constituted by two small square color objects. The number of measurements was $M = 4096$ ($M = N$), which allowed us to fulfill the Nyquist criterion. Eight central wavelengths, λ_0, were selected in the visible spectrum. The bandwidth of the corresponding spectral channels was 20 nm ($\lambda_0 \pm 10$ nm). Aside from the channels at the boundaries of the spectral range under consideration, the values of λ_0 correspond to peak emissions of commercial light-emitting diodes. The object spectral reflectance was determined again by means of the previously used white reference. The integration time of the spectrometer was set at 300 ms.

For each spectral channel, the off-line CS algorithm was resolved with the complete set of measurements. After a suitable filtering, the recovered matrix served as a reference (lossless) image $I_{ref}(i,j)$, where (i,j) indicates the location of an arbitrary image pixel. The reconstruction process was then repeated using decreasing fractions of the total number of pixels. In particular, the value of M was varied from 5 to 90% of N, and the fidelity of the reconstructed images was estimated by calculating the *mean square error* (MSE), given by

$$MSE = \frac{1}{N}\sum_{i}\sum_{j}\left[I(i,j) - I_{ref}(i,j)\right]^2, \tag{16.4}$$

where $I(i,j)$ is the noisy image obtained for a given value of M. The *peak signal-to-noise ratio* (PSNR) was used to evaluate the quality of the reconstruction. It is defined as the ratio between the maximum possible power of a signal and the power of the noise that affects the fidelity of its representation. In mathematical terms, [36]

$$PSNR = 10\log\left(\frac{I_{\max}^2}{MSE}\right) = 20\log(I_{\max}) - 10\log(MSE) \tag{16.5}$$

Here, $I_{\max}$ is the maximum pixel value of the reference image. For each spectral channel, the reference images were represented by 2^8 gray-levels, so $I_{\max} = 255$. Figures 16.6(a) and (b) show the curves for the MSE and the PSNR versus M for the different values of λ_0. Both figures point out that the image quality improves as the number of measurements grows and approximates to the Nyquist limit. However, it should be noted that the slope of both curves becomes visibly smoother for all spectral channels when $M \geq 0.4N$. In the case, for instance, of $\lambda_0 = 610$ nm, $MSE = 0.13I_{\max}^2$ and $PSNR = 28.72$ dB for $M = 0.4N$ (the PSNR for $0.9N$ is only somewhat greater, 29.10 dB).

Although this single-pixel camera acquires sequentially the spatial information of the input object, it allows collection of all the spectral content at once, in contrast to those cameras based on tunable band-pass filters, which perform a wavelength sweep to measure the spectral information. In addition, the number of channels, their spectral resolution, and the total wavelength range of the single-pixel system are those provided by the spectrometer working as detector. This fact makes possible to exploit the high performance of commercially available devices. Thus, the spectral system can, in principle, cover the whole VIS spectrum and part of the NIR range (up to 1.1 microns), while conventional multispectral systems require pixelated sensors specifically designed for the infrared range (like InGaAs cameras).

Apart from the detector, the illumination is another key element to ensure a minimum signal along the selected spectral range. The use of a high power Xe arc lamp provides a continuous

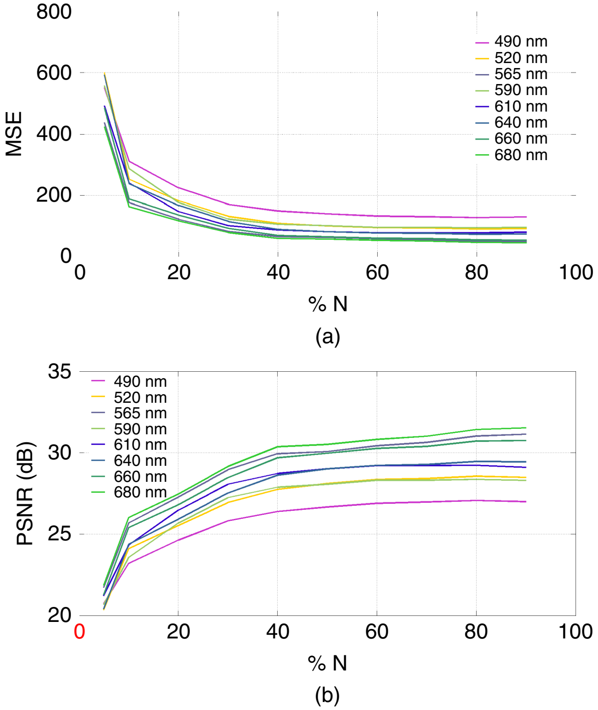

Figure 16.6 (a) MSE and (b) PSNR of the recovered images versus the number of measurements. Each curve corresponds to a spectral channel. *Source*: F. Soldevila, E. Irles, V. Durán, P. Clemente, M. Fernández-Alonso, E. Tajahuerce, and J. Lancis 2013, Figure 2. Reproduced with permission from Springer

and roughly uniform spectrum across the VIS region. However, the decreasing source irradiance at the "blue" side of the VIS spectrum, as well as the low reflectance of samples at that region, limits the spectral range to wavelengths higher than 500 nm.

This single-pixel multispectral camera presents a trade-off between image resolution and acquisition time. Increasing the illumination level or considering lower integration times (by a reduction of the spectral resolution) can make the acquisition time to drop by at least one order of magnitude. A comparable trade-off can be found in cameras based on acousto-optic or liquid crystal tunable filters, where the higher spectral resolution (number of channels), the longer acquisition time, with a strong dependence on the exposure time of the pixelated sensor used as a detector. A hyperspectral camera (i.e., a camera with more than 100 spectral channels) can take a few minutes in acquiring a data cube for image resolutions similar to those presented in this work [37].

16.5 Single-Pixel Spectropolarimetric Imaging

In certain applications, MI can be improved by adding spatially resolved information about the light polarization. Multispectral polarimetric imaging facilitates the analysis and identification of soils [38], plants [39], and surfaces contaminated with chemical agents [40]. In the field of biomedical optics, multispectral polarimetric imaging has been applied to the characterization of human colon cancer [41] or the pathological analysis of skin [42]. In many cases, polarimetric analysis can be performed by just including a linear polarizer in an imaging system to record images for various selected orientations of its transmission axis [42,43]. A simple configuration that includes two orthogonal polarizers integrated in a spectral system has been used for noninvasively imaging of the microcirculation through mucus membranes and on the surface of solid organs [43]. An illustrative example of a spectral camera with polarimetric capability is a system that combines an acousto-optic tunable filter with a liquid-crystal based polarization analyzer [44].

In this section we describe two different optical architectures for spectropolarimetric imaging. In the first one, polarimetry is performed by using a rotating linear analyzer in front of the detector, which leads to a linear polarization spectral imager. In the second one, the optical system is constituted by a fixed polarizer and two voltage-controlled variable retarders to spatially resolve the circular polarization component of light. In this way, this single-pixel multispectral system works as an imaging full-Stokes meter for each spectral channel.

16.5.1 Multispectral Linear Polarimetric Camera

A scheme of the multispectral linear polarimetric camera is depicted in Fig. 16.7. The optical system is similar to that described in the previous section, see Fig. 16.4(a), but now includes a linear polarizer. The sample scene is constituted by two square capacitors with a width of 7 mm. A xenon white light lamp is used again as illumination source. The light emerging from each

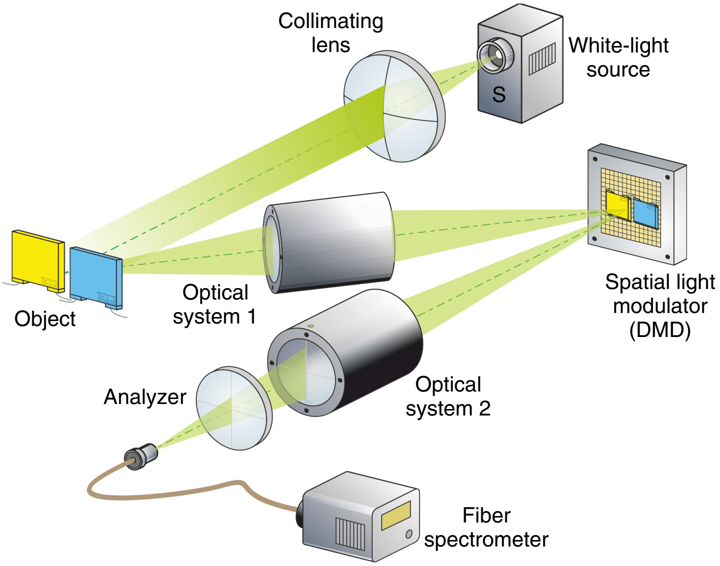

Figure 16.7 Optical system to obtain polarimetric multispectral imaging by using a single-pixel detector

Table 16.3 Technical specifications of the multispectral linear polarimetric camera

Wavelength range	470–700 nm
Number of channels	8
Image resolution	128 × 128 pixels
Compression ratio	5:1
Integration time	500 ms
Pixel pitch	43.2 μm

element of the scene had a different linear polarization. This spatial distribution of polarization was achieved by means of a linear polarizer located after the object, which had its area split in two parts, each of which with its transmission axis oriented at orthogonal directions (0 and 90°, respectively). The resolution of the patterns generated by the DMD was 128 × 128 unit cells ($N = 16384$) composed of 4 × 4 DMD pixels. The number of measurements was $M = 3249$, which corresponds to ~20% of N (i.e., a compression rate of 5:1). The integration time of the spectrometer was fixed to 500 ms. Eight central wavelengths λ_0 were selected in the VIS spectrum. The bandwidth of the channels was 20 nm ($\lambda_0 \pm 10$ nm). For each channel, four orientations of the polarization analyzer were sequentially considered in separated measurement series. The technical specifications of this camera are outlined in Table 16.3.

Figure 16.8 (Plate 27) shows the image reconstructions with the optical system in Fig. 16.7. Each column of the figure corresponds to a spectral channel and each row shows the results for a given orientation of the analyzer. A colorful image of the object is also shown (see Plate 27 in the plate section). This RGB image was made up from the data taken for the second configuration of the analyzer (45°). The result for 680 nm is presented by means of a gray-level image due to its proximity to the near infrared range.

The polarizer included in the single-pixel optical system in Fig. 16.7 limits the total spectral range, since the optical behavior of polarizing films is wavelength dependent. As a consequence, the upper boundary of the spectral range is ~700 nm. However, the use of high grade crystalline polarizers can solve this limitation.

16.5.2 Multispectral Full-Stokes Imaging Polarimeter

In principle, it is possible to obtain information about the spatial distribution of the Stokes parameters of light, S_i ($i = 0, \dots, 3$) from polarimetric images recovered for each spectral channel. In the previous optical system, as a linear polarizer is used as analyzer, the spatial distribution of S_0, S_1, and S_2 can be straightforwardly derived. However, a full Stokes polarimeter requires adding at least a linear retarder.

The scheme of a full-Stokes polarimeter is shown in Fig. 16.9. A white light beam generated by a xenon lamp is collimated by a lens and illuminates a sample object, whose image is formed on a digital micromirror device (DMD) by a pair of lenses. The light emerging from the DMD is guided to a single-pixel detector with the aid of a fourth lens. In order to achieve both polarimetric and spectral information, the single-pixel detector consists of two *liquid crystal variable retarders* (LCVR) (liquid crystal variable retarder from Meadowlark) with

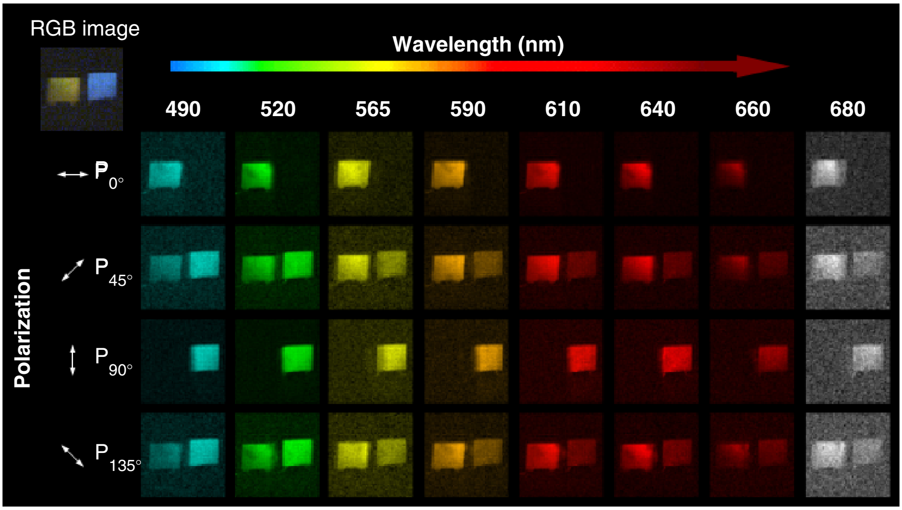

Figure 16.8 (Plate 27) Multispectral image cube reconstructed by CS algorithm for four different configurations of the polarization analyzer. The RGB image of the object is also included. In the VIS spectrum all channels are represented by pseudo-color images and a gray-scale representation is used for the wavelength closer to the NIR spectrum. *Source*: F. Soldevila, E. Irles, V. Durán, P. Clemente, M. Fernández-Alonso, E. Tajahuerce, and J. Lancis 2013, Figure 5. Reproduced with permission from Springer. *See plate section for the color version*

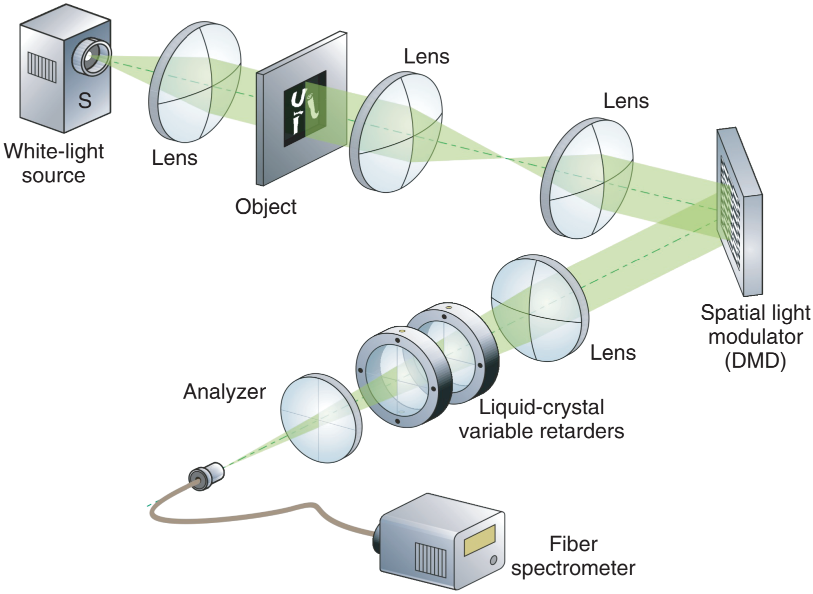

Figure 16.9 Scheme of the multispectral full-Stokes imaging polarimeter

their slow axis oriented at 45° and 0°, followed by a linear analyzer with its transmission axis oriented at 45° and a commercial fiber spectrometer (Black Comet CXRSR from StellarNet). Each LCVR is precalibrated to introduce controlled retardances in each chromatic channel of interest. The commercial fiber spectrometer is the same used in the preceding section.

By acquiring four images for different retardances of the LCVRs, it is possible to compute the Stokes parameters of each pixel of the scene. The CS algorithm provides an intensity map for the scene, which corresponds to the spatial distribution of the Stokes parameter S_0'. By using Stokes–Mueller calculus, it is possible to relate, for each pixel, the value of the Stokes vector with the measured irradiance S_0'. From the Mueller matrix expressions of a retarder wave plate and a linear polarizer, it is possible to show that the relationship between the recovered irradiance and the original Stokes parameters is

$$\begin{aligned} S_0'(2\delta_1, 2\delta_2) = {} & \frac{1}{2}S_0 + \frac{1}{2}\sin(2\delta_1)\sin(2\delta_2)S_1 \\ & + \frac{1}{2}\cos(2\delta_2)S_2 - \frac{1}{2}\cos(2\delta_1)\sin(2\delta_2)S_3, \end{aligned} \tag{16.6}$$

where $2\delta_1$ and $2\delta_2$ are the phase retardances introduced, respectively, by the two LCVRs. Equation 16.6 establishes an undetermined system with four unknown quantities (the Stokes parameters of the incident light). In order to solve that system, a minimum of four pairs of phase retardances must be applied to the two LCVRs. After the off-line reconstructions, the Stokes vector in each point of the scene is given by $\mathbf{S_0'} = \mathbf{M} \cdot \mathbf{S}$, where

$$\mathbf{M} = \frac{1}{2}\begin{pmatrix} 1 & \sin(2\delta_1^{(1)})\sin(2\delta_2^{(1)}) & \cos(2\delta_2^{(1)}) & -\cos(2\delta_1^{(1)})\sin(2\delta_2^{(1)}) \\ 1 & \sin(2\delta_1^{(2)})\sin(2\delta_2^{(2)}) & \cos(2\delta_2^{(2)}) & -\cos(2\delta_1^{(2)})\sin(2\delta_2^{(2)}) \\ 1 & \sin(2\delta_1^{(3)})\sin(2\delta_2^{(3)}) & \cos(2\delta_2^{(3)}) & -\cos(2\delta_1^{(3)})\sin(2\delta_2^{(3)}) \\ 1 & \sin(2\delta_1^{(4)})\sin(2\delta_2^{(4)}) & \cos(2\delta_2^{(4)}) & -\cos(2\delta_1^{(4)})\sin(2\delta_2^{(4)}) \end{pmatrix}. \tag{16.7}$$

The subscripts in the elements of **M** relate to each one of the LCVRs and the superscripts denote each one of the four acquisitions. The solution of this linear system provides the spatial distribution of the Stokes parameters.

As a direct application of the single-pixel spectral Stokes polarimeter, a photoelasticity measurement on a piece of polystyrene was carried out. In the process of fabrication, the piece of polystyrene is shaped in a certain form. Due to this, the material presents stresses that cause a spatial distribution of birefringence. This distribution can be seen when the piece is placed between crossed linear polarizers and illuminated with white light, as can be seen in Fig. 16.10.

The Walsh–Hadamard patterns addressed to the DMD had a resolution of 128 × 128 unit cells ($N = 16384$). Each unit cell was composed of 4 × 4 DMD pixels. The number of measurements was chosen to be $M = 3249$, which corresponds to ~20% of N (a measurement rate of 5:1). The integration time of each spectrometer measurement was set to 20 ms. These technical specifications of the camera shown in Fig. 16.9 are summarized in Table 16.4. In Fig. 16.11 (Plate 28) we show the experimental results of the distribution of the normalized Stokes parameters for eight chromatic channels, each one with 20 nm width ($\lambda_0 \pm 10$ nm). To simplify data display, image reconstructions are arranged in a table. Each column corresponds

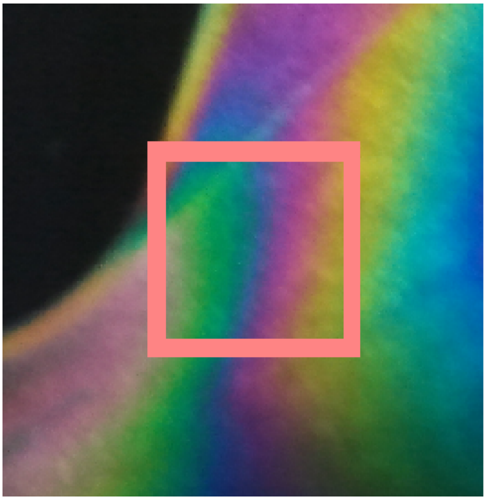

Figure 16.10 Color picture of the polystyrene sample. It is placed between two crossed linear polarizers and illuminated with white light. Color fringes are a consequence of the different states of polarization produced by the stress in the piece. The square indicates the region of interest imaged by the spectral camera

Table 16.4 Technical specifications of the multispectral full-Stokes imaging polarimeter

Wavelength range	450–730 nm
Number of channels	8
Image resolution	128 × 128 pixels
Compression ratio	5:1
Integration time	20 ms
Pixel pitch	43.2 μm

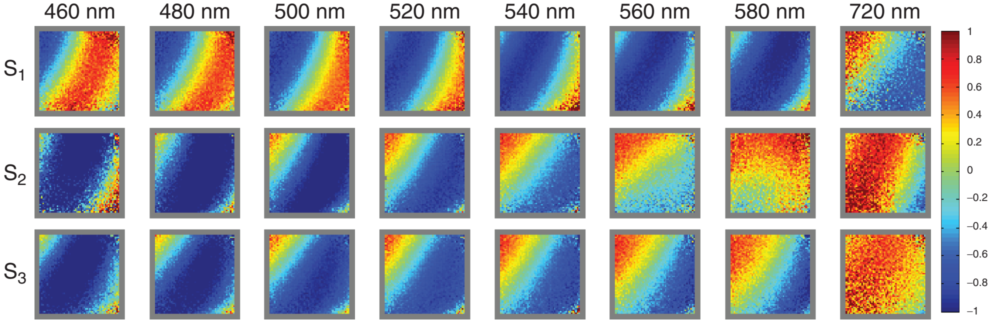

Figure 16.11 (Plate 28) Spatial distribution of the Stokes parameters of the polystyrene piece. Each distribution is represented by a pseudo-colored 128 × 128 pixels picture. The values range from −1 (blue) to 1 (red). *See plate section for the color version*

to a spectral channel and each row shows the spatial distribution of a normalized Stokes parameter.

To simplify data display, image reconstructions are arranged in a table. Each column corresponds to a spectral channel and each row shows the spatial distribution of a normalized Stokes parameter.

As can be seen in Fig. 16.11, the expected fringe distribution of the Stokes parameters is recovered, if we compare this result with that in Fig. 16.10. For wavelengths near the IR, reconstructions are a bit noisy. This is caused by the low amount of light the source emits in this zone of the spectrum, which causes the reconstructions on these channels to have lower SNR. This problem can be solved by increasing the integration time of the spectrometer, but this makes measurement times much greater and the reconstructions on the channels in the visible region of the spectrum do not improve their SNRs. Using a light source with a flatter spectrum will solve the quality drop near the IR region.

16.6 Conclusion

We have described several multi-dimensional single-pixel imaging techniques providing the spatial distribution of multiple optical properties of an input scene. In all cases, the key element of the optical system is a SLM that sequentially generates a set of intensity light patterns to sample the input scene. In this way, it is possible to apply the theory of compressive sampling to data acquired with a single-pixel sensor. In particular, we have described a single-pixel hyperspectral imaging polarimeter. This system is able to provide spatially resolved measurements of Stokes parameters for different spectral channels. In this case the spatial light modulator is a digital micromirror device, and the sensor is composed by polarizing elements followed by a commercial fiber spectrometer. Experimental results for color objects with an inhomogeneous polarization distribution show the ability of the method to measure the spatial distribution of the Stokes parameters for multiple spectral components.

Acknowledgments

This work has been partly funded by the Spanish Ministry of Education (project FIS2010-15746) and the Excellence Net from the Generalitat Valenciana about Medical Imaging (project ISIC/2012/013). Also funding from Generalitat Valenciana through Prometeo Excellence Programme (project PROMETEO/2012/021) is acknowledged.

References

[1] Brady D., *Optical Imaging and Spectroscopy*, 1st edn. John Wiley & Sons, Ltd, 2009.

[2] Weissleder R. and M. J. Pittet, "Imaging in the era of molecular oncology," *Nature*, vol. **452**, no. 7187, pp. 580–589, Apr. 2008.

[3] Tyo J. S., D. L. Goldstein, D. B. Chenault, and J. A. Shaw, "Review of passive imaging polarimetry for remote sensing applications.," *Appl. Opt.*, vol. **45**, no. 22, pp. 5453–5469, Aug. 2006.

[4] Brady D. J., M. E. Gehm, R. A. Stack, D. L. Marks, D. S. Kittle, D. R. Golish, *et al.*, "Multiscale gigapixel photography," *Nature*, vol. **486**, no. 7403, pp. 386–389, Jun. 2012.

[5] Geelen B., N. Tack, and A. Lambrechts, "A snapshot multispectral imager with integrated tiled filters and optical duplication," pp. 861314–861313, 2013.

[6] Zhao X. and F. Boussaid, “Thin photo-patterned micropolarizer array for CMOS image sensors,” *Photonics Technol.*, vol. **21**, no. 12, pp. 805–807, 2009.

[7] Candès E. and M. Wakin, “An introduction to compressive sampling,” *Signal Process. Mag. IEEE*, no. March 2008, pp. 21–30, 2008.

[8] Pratt W., J. Kane, and H. Andrews, “Hadamard transform image coding,” *Proc. IEEE*, vol. **57**, no. 1, 1969.

[9] Magalhães F., F. M. Araújo, M. V. Correia, M. Abolbashari, and F. Farahi, “Active illumination single-pixel camera based on compressive sensing,” *Appl. Opt.*, vol. **50**, no. 4, pp. 405–414, Feb. 2011.

[10] Duarte M. and M. Davenport, “Single-pixel imaging via compressive sampling,” *Signal Process.*, March 2008, pp. 83–91, 2008.

[11] Solomon J. E., “Polarization imaging,” *Appl. Opt.*, vol. **20**, no. 9, pp. 1537–1544, May 1981.

[12] Oldenbourg R., “A new view on polarization microscopy,” *Nature*, vol. **381**, no. 6585, pp. 811–82, Jun. 1996.

[13] Terrier P., V. Devlaminck, and J. M. Charbois, “Segmentation of rough surfaces using a polarization imaging system,” *J. Opt. Soc. Am. A. Opt. Image Sci. Vis.*, vol. **25**, no. 2, pp. 423–430, Mar. 2008.

[14] Demos S. G. and R. R. Alfano, “Optical polarization imaging,” *Appl. Opt.*, vol. **36**, no. 1, pp. 150–155, Jan. 1997.

[15] Baba J. S., J.-R. Chung, A. H. DeLaughter, B. D. Cameron, and G. L. Coté, “Development and calibration of an automated Mueller matrix polarization imaging system,” *J. Biomed. Opt.*, vol. **7**, no. 3, pp. 341–349, Jul. 2002.

[16] Laude-Boulesteix B., A. De Martino, B. Drévillon, and L. Schwartz, “Mueller polarimetric imaging system with liquid crystals,” *Appl. Opt.*, vol. **43**, no. 14, pp. 2824–2832, May 2004.

[17] de Boer J. F. and T. E. Milner, “Review of polarization sensitive optical coherence tomography and Stokes vector determination,” *J. Biomed. Opt.*, vol. **7**, no. 3, pp. 359–371, Jul. 2002.

[18] Song H., Y. Zhao, X. Qi, Y. T. Chui, and S. A. Burns, “Stokes vector analysis of adaptive optics images of the retina,” *Opt. Lett.*, vol. **33**, no. 2, pp. 137–139, Jan. 2008.

[19] Durán V., P. Clemente, M. Fernández-Alonso, E. Tajahuerce, and J. Lancis, “Single-pixel polarimetric imaging,” *Opt. Lett.*, vol. **37**, no. 5, pp. 824–826, Mar. 2012.

[20] Sabatke D. S., M. R. Descour, E. L. Dereniak, W. C. Sweatt, S. A. Kemme, and G. S. Phipps, “Optimization of retardance for a complete Stokes polarimeter.,” *Opt. Lett.*, vol. **25**, no. 11, pp. 802–4, Jun. 2000.

[21] Meadowlark Optics. *Liquid Crystal Polarimeter User Manual*. Available at www.meadowlark.com/store/PMI_Users_Manual_2.10.pdf, 2012.

[22] Davis S., R. Uberna, and R. Herke, “Retardance sweep polarimeter and method,” *US Pat. 6,744,509*, vol. **2**, no. 12, 2004.

[23] Durán V., J. Lancis, E. Tajahuerce, and Z. Jaroszewicz, “Cell parameter determination of a twisted-nematic liquid crystal display by single-wavelength polarimetry,” *J. Appl. Phys.*, vol. **97**, no. 4, p. 043101, 2005.

[24] Brosseau C., *Fundamentals of Polarized Light: A Statistical Optics Approach*, 1st edn. John Wiley & Sons, Inc., 1998.

[25] Boreman G. D., “Classification of imaging spectrometers for remote sensing applications,” *Opt. Eng.*, vol. **44**, no. 1, p. 013602, Jan. 2005.

[26] Stamatas G. N., M. Southall, and N. Kollias, “In vivo monitoring of cutaneous edema using spectral imaging in the visible and near infrared,” *J. Invest. Dermatol.*, vol. **126**, no. 8, pp. 1753–60, Aug. 2006.

[27] Hamilton S. J. and R. A. Lodder, “Hyperspectral imaging technology for pharmaceutical analysis,” in *Proc. SPIE 4626, Biomedical Nanotechnology Architectures and Applications*, pp. 136–147, 2002.

[28] Scholl J. F., E. K. Hege, M. Hart, D. O’Connell, and E. L. Dereniak, “Flash hyperspectral imaging of non-stellar astronomical objects,” in *Proc. SPIE 7075, Mathematics of*

Data/Image Pattern Recognition, Compression, and Encryption with Applications XI, vol. **7075**, p. 70750H–70750H–12, 2008.

[29] Dale L. M., A. Thewis, C. Boudry, I. Rotar, P. Dardenne, V. Baeten, and J. A. F. Pierna, "Hyperspectral imaging applications in agriculture and agro-food product quality and safety control: a review," *Appl. Spectrosc. Rev.*, vol. **48**, no. 2, pp. 142–159, Mar. 2013.

[30] Mehl P. M., Y.-R. Chen, M. S. Kim, and D. E. Chan, "Development of hyperspectral imaging technique for the detection of apple surface defects and contaminations," *J. Food Eng.*, vol. **61**, no. 1, pp. 67–81, Jan. 2004.

[31] Soldevila F., E. Irles, V. Durán, P. Clemente, M. Fernández-Alonso, E. Tajahuerce, and J. Lancis, "Single-pixel polarimetric imaging spectrometer by compressive sensing," *Appl. Phys. B*, vol. **113**, no. 4, pp. 551–558,2013.

[32] Sampsell J. B., "Digital micromirror device and its application to projection displays," *J. Vac. Sci. Technol. B Microelectron. Nanom. Struct.*, vol. **12**, no. 6, p. 3242, Nov. 1994.

[33] Vila-Francés J., J. Calpe-Maravilla, J. Muñoz-Mari, L. Gómez-Chova, J. Amorós-López, E. Ribes-Gómez, and V. Durán-Bosch, "Configurable-bandwidth imaging spectrometer based on an acousto-optic tunable filter," *Rev. Sci. Instrum.*, vol. **77**, no. 7, p. 073108, 2006.

[34] Zou X., J. Shi, L. Hao, J. Zhao, H. Mao, Z. Chen, *et al.*, "*In vivo* noninvasive detection of chlorophyll distribution in cucumber (Cucumis sativus) leaves by indices based on hyperspectral imaging," *Anal. Chim. Acta*, vol. **706**, no. 1, pp. 105–112, Nov. 2011.

[35] Mather J., "Spectral and XYZ color functions," 2005. [Online]. Available at: www.mathworks.com/matlabcentral/fileexchange/7021-spectral-and-xyz-color-functions (accessed December 6, 2013).

[36] Pratt W. K., *Digital Image Processing*, 4th edn. John Wiley & Sons, Inc., 2007.

[37] Zuzak K. J., M. D. Schaeberle, E. N. Lewis, and I. W. Levin, "Visible reflectance hyperspectral imaging: characterization of a noninvasive, *in vivo* system for determining tissue perfusion," *Anal. Chem.*, vol. **74**, no. 9, pp. 2021–2028, May 2002.

[38] Coulson K. L., "Effects of reflection properties of natural surfaces in aerial reconnaissance," *Appl. Opt.*, vol. **5**, no. 6, pp. 905–917, Jun. 1966.

[39] Vanderbilt V. C., L. Grant, L. L. Biehl, and B. F. Robinson, "Specular, diffuse, and polarized light scattered by two wheat canopies," *Appl. Opt.*, vol. **24**, no. 15, pp. 2408–2418, Aug. 1985.

[40] Haugland S. M., E. Bahar, and A. H. Carrieri, "Identification of contaminant coatings over rough surfaces using polarized infrared scattering," *Appl. Opt.*, vol. **31**, no. 19, pp. 3847–3852, Jul. 1992.

[41] Pierangelo A., A. Benali, M.-R. Antonelli, T. Novikova, P. Validire, B. Gayet, and A. De Martino, "*Ex-vivo* characterization of human colon cancer by Mueller polarimetric imaging," *Opt. Express*, vol. **19**, no. 2, pp. 1582–1593, Jan. 2011.

[42] Zhao Y., L. Zhang, and Q. Pan, "Spectropolarimetric imaging for pathological analysis of skin," *Appl. Opt.*, vol. **48**, no. 10, pp. D236–246, Apr. 2009.

[43] Groner W., J. W. Winkelman, A. G. Harris, C. Ince, G. J. Bouma, K. Messmer, and R. G. Nadeau, "Orthogonal polarization spectral imaging: a new method for study of the microcirculation," *Nat. Med.*, vol. **10**, no. 10, pp. 1209–1212, 1999.

[44] Gupta N. and D. R. Suhre, "Acousto-optic tunable filter imaging spectrometer with full Stokes polarimetric capability," *Appl. Opt.*, vol. **46**, no. 14, pp. 2632–2637, May 2007.